A Mark III panel subjected to a flip-through wave impact: results from the *Sloshel* project

L. Brosset[(1)], W. Lafeber[(2)], H. Bogaert[(2)], M. Marhem[(1)], P. Carden[(3)], J. Maguire[(3)]
[1]GTT (Gaztransport & Technigaz), Saint-Rémy-lès-Chevreuse, France
[2]MARIN, Hydro Structural Services, Wageningen, The Netherlands
[3]Lloyd's Register EMEA, London, United Kingdom

ABSTRACT

Within the Sloshel Joint Industrial Project, a new full scale wave impact test campaign has been carried out in April 2010. Unidirectional focused waves were generated in a flume in order to impact a rigid wall in which an instrumented Mark III LNG containment system panel had been embedded. The wall was entirely covered with the Mark III corrugated membrane in the same way as on board a LNG carrier.

During one of the last tests of the campaign a flip-through type of impact was generated and very high local pressures were measured. The horizontal small corrugations of the membrane were significantly deformed but no permanent deformation of the foam was observed by initial visual inspection. After removing the Mark III panel and cutting it into small blocks, no discernible cracking, no discernible permanent deformation and no discernible change of the initial properties were observed.

This paper describes the main lessons obtained from this flip-through impact, through measurements related to the hydrodynamic loads, and through the structural response of the different components of the Mark III panel.

KEY WORDS: Sloshing, LNG carrier, Mark III, Corrugation, Containment System, Flip-Through, impact pressure, Sloshel

INTRODUCTION

The aim of the Sloshel full scale Mark III tests was to study some key issues related to sloshing impacts in tanks of Mark III LNG vessels through impact tests of breaking waves in a flume. Although obviously not identical to the real conditions, the conditions induced by impacts of breaking waves in a flume with water and air on a real Mark III containment system are considered to be relevant for studying fluid-structure interactions, scaling effects by comparison with a previous test campaign at scale 1:6 and wave–corrugation interactions. These tests also enabled the building of a reference data base for validation of numerical simulations.

As the loads generated by the water are almost twice as large as those generated by LNG for similar waves due to the ratio of densities, caution was taken in order to not damage the membrane or the containment system before having stored enough data. The wooden-wedge-reinforced version of the membrane was used and only large air-pocket type or slosh type of impacts (inducing large but not extreme loads) were generated at first. These types of impacts, described in Brosset et al (2009), are believed to be the most representative of sloshing impacts for low and partial fill levels in tanks of LNG carriers.

After 139 tests with such waves, without any discernible deformation of the corrugations, it was decided to generate intentionally a flip-through type of impact, less likely to occur onboard a ship but potentially capable to deform the corrugations and to damage the foam or the plywood plates of the Mark III panel.

During test 140 a real flip-through impact was created, inducing a maximum measured pressure of 56 bar, the highest ever measured during the different campaigns of the Sloshel project. The horizontal corrugations of the membrane were significantly deformed with a maximum deflection of 5 mm. No permanent deformation of the foam was observed by initial visual inspection. After two subsequent tests generating moderate impacts, it was decided to end the campaign in order to allow a careful check of the Mark III panel, including search for cracks after cutting the panel into small blocks and material tests. No residual deformation of the foam and no discernible change of the initial mechanical properties were observed.

This paper describes in detail test 140, through the numerous measurements (pressures, strains, forces) and high speed videos recorded, related to both the loads and the response of the containment system including the corrugations. Reasons are proposed to explain why the foam was not crushed after the panel withstood a maximum pressure of 30 bar while its notional capacity is only 14 bar at ambient temperature in static conditions.

TEST SET-UP

The full scale Mark III tests were carried out in the outdoor Delta flume operated by Deltares in The Netherlands. The flume is 240 m long, 7 m high and 5 m wide. At one end it features a piston-type second order wave making system. Details of the set-up are given by Kaminski and Bogaert (2010). For the sake of simplicity, only the elements that are relevant to the present paper are described in the section below.

General set-up

A transverse concrete test wall was placed 145 m from the wave maker. A horizontal steel test panel was embedded into the test wall, enabling the mounting of two instrumented blocks at a height in between 5.0 m and 6.0 m above the bottom of the flume as indicated in **Figure 1**. The two blocks were 1.2 m wide and 1.0 m high. The first one, on the left in **Figure 1**, was a thick block of aluminium. The second one, on the right in **Figure 1**, was a Mark III panel cut in order to fit within the opening (1.2 m wide instead of 3 m originally). The panel was assembled from components delivered by a Mark III certified manufacturer. The two blocks were bonded at their back sides to metallic plates (force plates) lying on load cells. The Mark III panel was glued on the force plate using horizontal mastic ropes running over its whole width and spaced every 100 mm.

The test wall was completely covered by the Mark III corrugated membrane in the same way as on board a LNG carrier, as shown in **Figure 1**. The large corrugations were set vertically. This choice was motivated by the fact that, when deformed corrugations have been observed on board LNG carriers in the lower part of the tanks, they were most of the time located on the longitudinal bulkheads. As the tests were performed with water, thus with a density more than twice the density of LNG, the reinforced version of the Mark III membrane was used. In this version, installed recently on board some Mark III ships, the large corrugations have ribs and all corrugations are strengthened by wooden wedges.

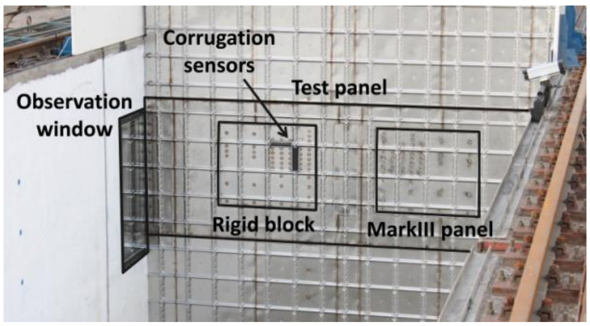

Figure 1 - Test set-up of full scale Mark III tests. Test panel, rigid block, Mark III panel, corrugation sensors and observation window.

Instrumentation

Each block was instrumented with 52 pressure sensors placed flush on its surface running through and welded to the membrane. The configurations of sensors on both blocks were symmetrical to the middle vertical line of the wall. The sensors can be distinguished on **Figure 1**. These configurations with the numbering of the sensors are detailed in **Figure 2**. The letters 'R', 'M' and 'P' stand respectively for 'Rigid block', 'Mark III block' and 'Pressure sensor'.

Two especially-designed *corrugations sensors* were developed by MARIN. Such sensors have the shape of real corrugations and were set-up on the wall instead of the original corrugations. Each sensor measured two forces exerted by the flow on each side of the corrugation, perpendicular to the corrugation in the wall plane. The forces are positive when oriented towards the centre of the corrugation. A vertical and a horizontal corrugation sensor were set up on the rigid block. They can be readily distinguished on **Figure 1**.

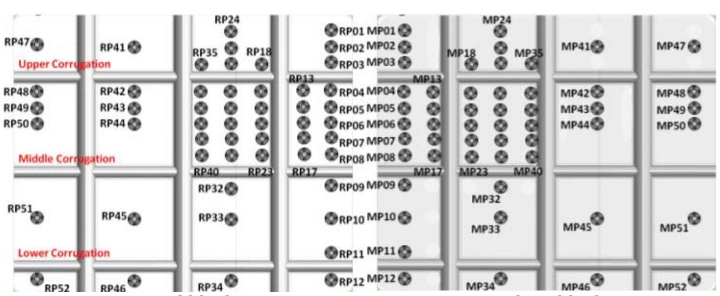

Rigid block *Mark III block*

Figure 2 - Configuration of pressure sensors on Rigid block and Mark III panel.

The Mark III panel was also instrumented with strain gauges and accelerometers on (1) the inside of the plywood cover plate, (2) the triplex membrane and (3) both sides of the bottom plywood plate. **Figure 3** shows the sensor configurations for both plywood plates. The letters 'S' and 'A' stand respectively for 'Strain gauge' and for 'Accelerometer'.

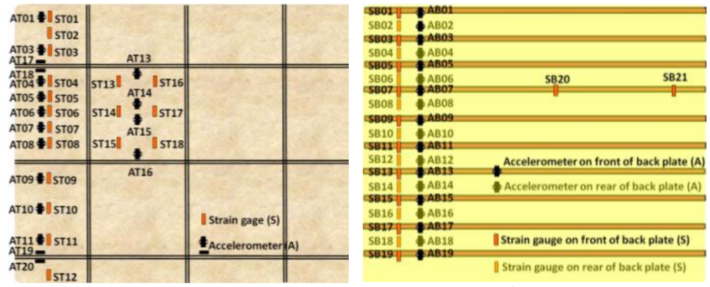

Underneath the top plate *Both sides of the bottom plate*

Figure 3 – Configuration of accelerometers (black) and strain gauges (orange) for the top and the bottom plates of Mark III block. Top views.

Transient foam displacements were captured by an optical system based on two high speed cameras observing a section of the foam coated by a speckle raster. The two cameras were fixed as rigidly as possible at the left upper side of the Mark III panel inside the wall. The speckle pattern and the two high speed cameras observing the pattern are shown in **Figure 4**. The area observed by the cameras spans the whole thickness of the foam on a total height of 250 mm in between h1=5.650 m and h2=5.900 m. This area is centred on the upper corrugation of the Mark III block. It is the area targeted to be impacted by the crests of the waves and to withstand the highest pressures. This area is also covered by the largest density of pressure sensors and strain gauges.

An observation window was fitted in the longitudinal flume wall, adjacent to the impacted wall, at the same height as the test panel. The window was 1.5 m high and 1 m wide and can be seen on the white painted flume wall in **Figure 1**. Behind the thick glass of the observation window three high speed video cameras were installed. For each impact, the first camera (HSC1) recorded the full view, the second camera (HSC2) focused on the area in between the middle and the upper corrugations and the third camera (HSC3) zoomed closer around the upper corrugation.

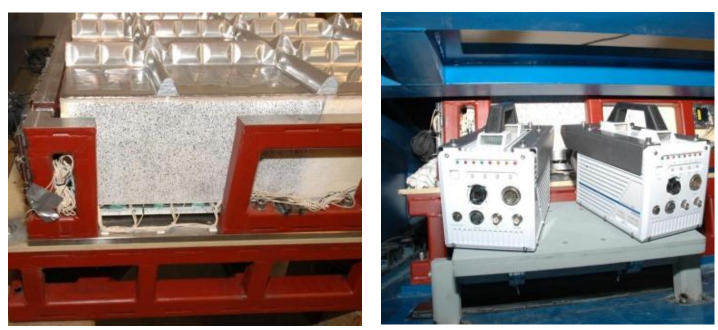

Figure 4 - Speckle pattern at the left side of the Mark III panel (left), and high speed cameras observing the speckle pattern (right).

The data acquisition system for the pressure sensors, strain gauges, accelerometers and load cells sampled at 50 kHz. The cameras observing the displacements of the foam section recorded at 15 kHz. The three cameras inside the observation window were recording respectively at 5 kHz, 5 kHz and 1.2 kHz. All the cameras were synchronized with the data acquisition system.

The maximum measured pressure (55.6 bar) was obtained on sensor RP36 of the rigid block. The instant for which the maximum is reached is taken as the origin of time throughout this paper.

HYDRO-DYNAMICS AND LOADS

All impacting waves during this campaign were generated by a focusing technique (see Hofland et al., 2010 and Kimmoun et al., 2010). Wave packets were generated by the paddle in order to meet at a theoretical focal point. The main parameter enabling the adjustment of the shape of the wave just before the impact was the location of the focal point with regards to the wall. Test 140 was a Flip-Through type of impact, which is considered as a limit case in between the air-pocket type and the slosh type of impact (see Kaminski et al., 2011, Bogaert et al., 2010, Brosset et al., 2009). It is difficult to realize such a flip-through impact in laboratory conditions. Here, the waves have been designed very carefully with an accurate tuning of the parameters at first in a small flume in order to master better the repeatability of the global flow (shape of the wave just in front of the wall) and to obtain as high a pressure as possible. It is considered that this kind of wave is very unlikely to happen in real (in-service) conditions. Nevertheless it is interesting because it brings insight about fluid-structure interaction in highly dynamic conditions.

The Flip-Through impact

Figure 5 shows three pictures recorded by the high speed camera HSC1 inside the observation window at three instants just before the impact. There is a time step of 30 ms between the pictures.

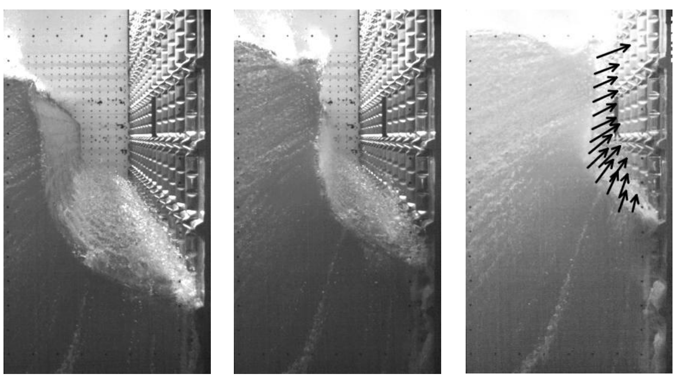

t= -75.6 ms t= -45.6 ms t= -15.6 ms

Figure 5 – Wave shape for test 140 just before the impact (Camera HSC1). The black arrows represent the velocities of the bubbles inside the water near the free surface. V_{max}=8 m/s.

The first observation that can be made from these pictures is that, as intended, the flow is globally 2D, if the boundary effects on the two longitudinal walls are disregarded. Actually, a close look at the pictures shows that the liquid section close to the observation window is slightly delayed, by a few centimetres compared to the section on the opposite wall. This is confirmed by the analysis of the pressure signals on the horizontal lines of sensors. The signal pattern is globally reproduced from the right to the left but with an almost constant delay of 2.3 ms from pressure sensor column of sensor MP47 (right part of the Mark III block) to column of sensor RP47 (left part of the rigid block). Another consequence is that what is seen from the observation window happens around 2 ms after it has happened on the Mark III block and 1 ms after it has happened on the rigid block.

There are two main global processes that are progressing together: the run-up of the wave trough and the forward moving of an almost vertical wave front.

The run-up process of the wave trough is a general process that would also appear for Air-pocket-type or Slosh-type of impacts. This process mitigates the impact whatever the type because it converts smoothly a part of the horizontal momentum of the wave to a vertical momentum. For a Flip-Through impact the speed of the run-up is higher than for the two other types. Here the maximum vertical velocity of the trough is 4.7 m/s. If the wall were smooth (without corrugations), this run-up process would not induce any significant load on the wall until the wave front is close enough. These conditions have been called *restricted wave trough* in Bogaert et al. (2010). In these conditions, an upward vertical jet would start building from the trough and a pressure pulse would arise from the root of the jet at the wave trough intersection with the wall and travel with the wave trough along the wall. Until these restricted trough conditions are met, the free surface of the trough intersects the wall perpendicularly.

The moving forward of the wave front is also a general process for all types of waves. It can lead to an overturning crest for an Air-Pocket type of impact which would hit directly the wall. The maximum horizontal speed of the front was 8 m/s for test 140. As both the wave front is moving forward and the trough is running up, the space filled by the air in between the front, the trough and the wall is decreasing quickly. This induces an upward vertical air flow. This flow shears the free surface, drawing drops of water out of the bulk of liquid and creating strong irregularities on the free surface and a spray around it. This instability of the free surface is known as the Kelvin-Helmotz instability (see Drazin, 2004) and is believed to be the main cause of the non-repeatable impact pressure measurements on the wall when repeating accurately the impact conditions. The speed of the extracted drops can be evaluated from high speed camera records and gives an estimation of the air flow vertical velocity. Here the maximum vertical speed of air is evaluated at 50 m/s. Another influence of the air flow is to shape the free surface. For test 140 there is no clear crest. The action of the air jet helps preventing the overturning of the crest.

The loading processes

The trough run-up and the forward move of the wave front are global processes. At each time the trough passes by a corrugation, the same local phenomena happen:

1. immersion of the corrugation (water entry of the corrugation in a reference system linked to the corrugation) and separation of the flow;
2. reattachment of the flow to the wall;
3. entrapment of a small air pocket in between the corrugation and the reattachment point, and compression of this air pocket.

These local phenomena are quite smooth as long as the trough is unrestricted, and do not generate significant loading of the wall or the corrugations. When the wave front is very close, these phenomena become stronger and generate new local phenomena that interact also with the corrugations. These phenomena are detailed in this subsection through the video recordings, the pressure measurements and the force measurements on the horizontal corrugation sensor. For the sake of simplicity, only pressure signals of sensors RP1 to RP8 of the rigid block (see **Figure 2**) are given in this section to illustrate the different phenomena. These sensors, located on the first right column of sensors in the rigid block, give the longest

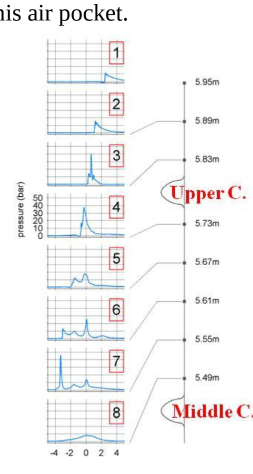

Figure 6 – Pressure signals at RP1 to RP8.

series of working sensors in a column.

As there is a good 2D behavior of the wave, with good duplication of the signal patterns horizontally (at least on the rigid block), this column of sensors is representative of the loading processes on the whole rigid block. The eight pressure signals and the locations of the related sensors are given in **Figure 6**.

- **Direct impact due to the reattachment of the trough**

When the trough is restricted by the close presence of the wave front, the reattachment of the flow, after separation imposed by the run-up along the corrugation, may be very violent. This is the case during test 140 for the reattachment following the separation from the middle horizontal corrugation of the blocks, as illustrated by **Figure 7** by a succession of pictures taken by camera HSC2 at very short time intervals.

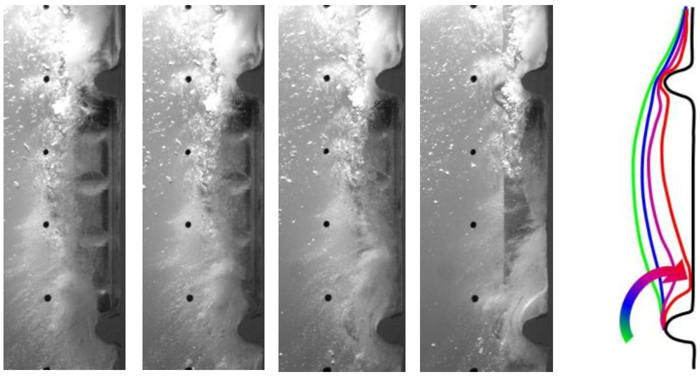

t= -8.22 ms t= -6.62 ms t= -5.22 ms t= -3.22 ms Sketch of free surf.

Figure 7 – Separation and reattachment of the flow after the run-up along the middle corrugation (HSC2).

This reattachment leads to a local impact close to sensor row of RP7 with a horizontal velocity evaluated from the videos at 16 m/s. The maximum impact pressure recorded for this local impact is 46.1 bar at RP7. This kind of hydrodynamic impact is very localized: the sensors RP6 and RP8, only 60 mm away from RP7, felt the consequences of the hydrodynamic impact (described later) but not directly the pressure peak. It is also very short: around 0.5 ms at RP7.

The reattachment of the flow leads to the entrapment and the compression of a small air pocket in between the middle corrugation and the impact point. Sensor RP8 is located inside this small air pocket. The boundary of the pocket is clearly visible on the picture at instant t= -3.22 ms of **Figure 7**. As a consequence the white cloud around the pocket must be considered as aerated water.

There is also such a reattachment a few milliseconds later after the separation due to the run-up along the upper horizontal corrugation of the blocks. The reattachment is not obvious from the videos but is logically expected and can be deduced from the pattern of the pressure signals at sensor RP3. **Figure 8** shows the pressure signals at RP8, RP7 and RP3.

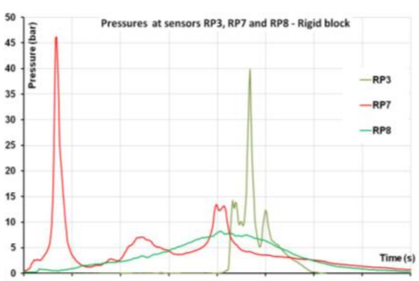

Figure 8 – Pressure signals at RP3, RP7 and RP8. Impact pressures due to the reattachments after separation at middle (RP7) and upper (RP3) corrugation. Pressure in the entrapped gas pocket (RP8).

The reattachment of the flow to the wall is a direct impact that generates locally a pressure wave into the liquid and a strain wave into the impacted structure. The pressure wave into the liquid after the first reattachment is clearly visible on the high speed videos. As the water is aerated, the color of the water becomes darker when the front of the wave is passing by, because the bubbles are compressed. This reason has been clearly demonstrated by a close observation of large bubbles crossed by the pressure wave. The speed of the pressure wave has been evaluated around 250 m/s from the videos. This value corresponds to a speed of sound in water with 1% of aeration. With such a speed of sound of the aerated water and the impact velocity of 16 m/s already given, the acoustic pressure on a rigid wall would be 40 bar. The maximum impact pressure of 46.1 bar obtained on the rigid block is in line with this scenario.

The direct impacts due to the reattachment of a restricted wave trough after separation from a horizontal corrugation are very much like wave crest impacts. They lead to non-traveling pressure pulses of large amplitude and short duration, much localized (radius of less than 60 mm here). Such events are thus difficult to capture and might be missed by the network of pressure sensors although actually present.

- **Vertical jet building from the reattaching trough**

After each impact due to a reattachment, a vertical upward liquid jet is building from the impact point. The development of this jet after the first reattachment around pressure sensor RP7 is described in **Figure 9** by a succession of pictures taken by HSC2 at very short time intervals.

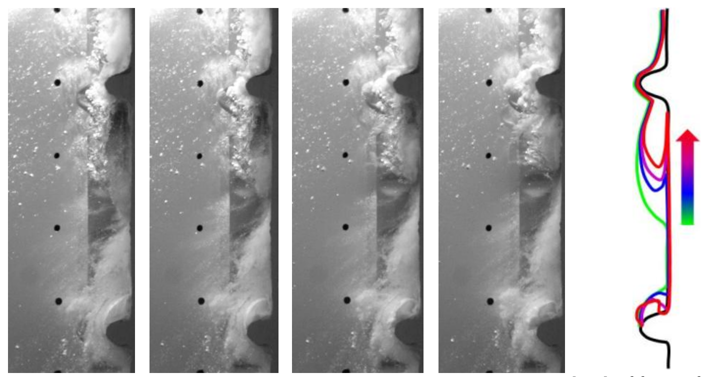

t= -3.02 ms t= -2.42 ms t= -1.82 ms t= -1.22 ms Sketch of free surf

Figure 9 – Building upward vertical jet from the reattaching trough (HSC2).

The root of the jet is located at a point on the wall which is moving upwards because the wave front is still feeding the impact area. This area is thus becoming larger. Close to this point, the velocities in the fluid have to take a very sharp turn, which leads to a pressure pulse on the wall traveling upwards with the point. This traveling pulse is very much like the traveling pressure pulse induced by a drop of a wedge into water initially at rest, a good approximation of which is given by the so-called Wagner solution (see Wagner, 1932).

Such a traveling pulse is captured by pressure sensors RP6 and RP5 due to the liquid jet building from the first reattachment above the middle corrugation and afterwards by pressure sensors RP2 and RP1 due to the liquid jet building from the second reattachment above the upper corrugation.

Figure 10 shows the pressure signals at RP6, RP5, RP2 and RP1. Only the first rise and decrease of the pressure signals at RP6 and RP5 is explained by the traveling pulse due to the building jet. From these signals, a vertical velocity of the root of the jet can be estimated, which is around 60 m/s for the first event and around 43 m/s for the second event.

Figure 10 – Pressure signals at RP6, RP5, RP2 and RP1. Traveling pulses at the root of vertical jets following the reattachment above the middle corrugation (RP6 and RP5) and above the upper corrugation (RP2 and RP1).

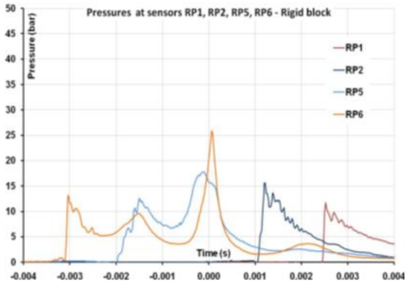

- **Direct impact of the jet on the upper corrugation**

The upward jet induced by the reattachment will hit the upper corrugation. At the same time the gas below the corrugation is still escaping, turning around the corrugation. These processes are described in **Figure 11** by a succession of pictures taken by camera HSC2 at very short time intervals.

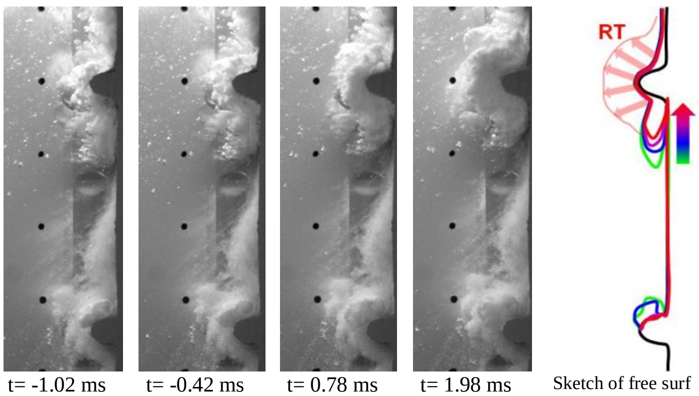

Figure 11 – Impact of the jet on the upper corrugation. Compression of the escaping gas below the corrugation until a sudden Rayleigh-Taylor (RT) gas/liquid mixing process (HSC2).

The volume of air in between the upper corrugation, the trough and the front is decreasing quickly. However the gas is not entrapped and can escape along the corrugation. The white cloud that is seen in the first three pictures of **Figure 11** is due to the Kelvin-Helmotz instability of the free surface induced by the air jet tangential to the free surface.

Two sensors can help to understand in more in depth what happens locally - they are the bottom part of the horizontal corrugation sensor and the pressure sensor RP4 just under the upper corrugation. Their signals are shown on **Figure 12**.

Figure 12 – Pressure signals at RP4 and force signal at the bottom part of the horizontal corrugation sensor.

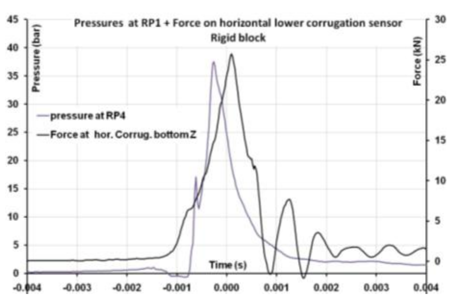

It can be seen that there are two parts in the pressure signal at RP4. The first slope is due to the traveling pressure pulse at the root of the jet. So after passing along sensors RP6 and RP5 (see **Figure 10**), the trough is reaching sensor RP4. There is no increase of the pressure before this sharp raise which confirms that the sensor was not within an entrapped air pocket and the air was still able to escape along the corrugation.

The force on the corrugation sensor starts rising before the root of the jet reaches sensor RP4 although there is no gas pocket compression. Hence, this first rise is due to the impact of the jet on the root of the corrugation. The jet is very thin and cannot alone be responsible for the following rise of the force. A possible scenario is that the thin layer of gas flowing below the corrugation starts to be highly compressed because the gas cannot escape quickly enough. This scenario would explain that very suddenly during the rise of the force on the corrugation, a new cloud of bubbles appears as can be seen on the fourth picture of **Figure 11** (t=1.98 ms). It looks as though the layer of gas explodes, penetrating the free surface by means of bubbles and preventing reaching an even higher pressure. This intrusion of the gas through a liquid free surface is known as the Rayleigh-Taylor process (see Drazin, 2004). It appears as a mitigating process that should be studied carefully in the context of sloshing.

- **Other phenomena**

If one wishes to understand any details of the pressure signals on the rigid block, one needs to be aware that, at any point of the liquid, there is not only the influence of local events but also an influence of remote events. This influence decreases rapidly with the distance ($\sim 1/r^2$). When the liquid is considered as incompressible the information is supposed to be transmitted instantaneously. In the reality, it is traveling continuously through the liquid at the speed of sound by means of pressure waves from one pressure source to any remote point.

Four main elementary loading processes have been described above: the direct impact while the surrounding gas can escape freely, the traveling pulse at the root of a jet, the compression/expansion of an entrapped gas pocket, and the quick compression of a thin jet of escaping gas. Most of the time, only the last three processes are directly measured by pressure sensors. The direct impact process is much localized and it is unlikely to have a sensor just at the right point. What is measured when the phenomenon is captured by a sensor is the remote influence transmitted from the source by a pressure wave. This is likely to be the case for pressure peaks measured at RP3 and RP7 shown on **Figure 8**. This also implies that the maximum pressure measured is not necessarily the maximum pressure actually reached in the vicinity.

The second bump of the pressure signal at RP5 and the third bumps of pressure signals at RP6 and RP7 can also be considered as the remote influence of the final impact on the corrugation. This can be seen more clearly on **Figure 13** gathering all pressure time traces of sensors RP1 to RP8.

The analysis of the remote influence of a loading process is made complex by the fact that these loading processes are very local and some particular events may have occurred that were not captured by the high speed camera recordings. Moreover the level of aeration in the vicinity of the wall can quickly vary in space and in time (presence of bubble clouds for instance), which induces strong variations of the speed of sound.

- **Summary**

All pressure signals of sensors RP1 to RP8 are gathered on **Figure 13**.

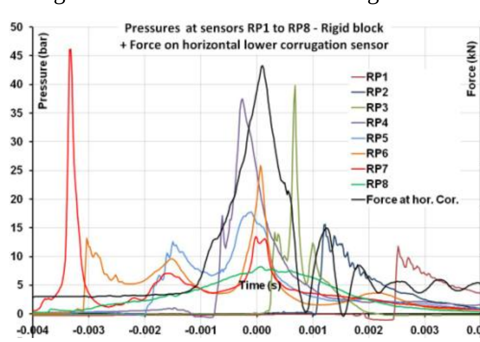

Figure 13 – Pressure signals at sensors RP1 to RP8 and force signal at the bottom part of the horizontal corrugation sensor.

The different parts of the pressure signals recorded during test 140 have been induced by only four different types of elementary local loading processes plus remote influences propagated by pressure waves. These local phenomena are similar as those already seen during drop-tests of wedges into water initially at rest in case the surface of the dropping wedge includes transverse corrugations or raised edges. For more details about these local loading processes, refer to Lafeber et al., 2011.

HYDRO-STRUCTURAL INTERACTION

The Mark III block was instrumented with many sensors. In this section, we will focus on the top left part of the block, from the middle corrugation to the top and from its left section to the first vertical corrugation (see **Figure 1**, **Figure 2** and **Figure 3**). As the top part was the targeted impact area for all tests, supposed to withstand the highest loads, the left section of this top part was watched by the optical system (two high speed cameras inside the wall) and the top left area was instrumented with the highest density of sensors.

Figure 14 shows the locations of these different sensors and their numbering, including *P*ressure sensors (M*P*), *S*train gauges (*S*T) and *A*ccelerometers (*A*T) behind the *T*op plate, *S*train gauges (*S*B) and *A*ccelerometers (*A*B) on both sides of the *B*ottom plate. The section of the foam as seen by the optical system (in grey) corresponds to a state at rest. The triplex membrane is represented by a vertical line - it could not be detected from the pictures of the optical system. The top and back plates have also been added. The top plate is out of shot but the back plate is in shot of the two high speed cameras.

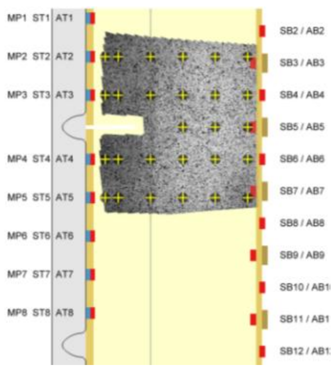

Figure 14 – Instrumentation of the top left part of the Mark III block. Pressure sensors in blue. Strain gauges and accelerometers, both in red.

The pictures from the optical system presented in this paper have been corrected from optical distortions and rigid body motion. After post-processing, the displacements and thus the strains can be derived from the pictures at every point. A grid of reference points has been added on **Figure 14**. The time traces of the normal strains presented later have been post-processed at these locations.

Maximum deflections in the Mark III panel

The maximum transient displacement of the foam normal to its thickness is 2.6 mm and is obtained just under the slit at t=-0.29 ms, almost when the maximum pressure is reached on the Mark III block. The maximum normal strain is 1.5%. At the same time the foam is sheared due to the upward vertical force exerted by the flow on the corrugation and transmitted to the top plate. The maximum vertical displacement is 1.4 mm. These values are relatively low compared to the threshold for permanent deflection of the foam as it will be described in the next section dedicated to Strength.

Figure 15 shows the deformed foam and back plate at this instant with a magnification factor of ten. The foam is colored according to the level of normal strains, as post-processed from the pictures recorded by the optical system.

The relaxation slit in the primary foam underneath the upper corrugation avoids the generation of high shear stresses in the top plate. As a consequence there is a higher concentration of normal stresses in the primary barrier just below the upper corrugation. The presence of the very stiff mastic ropes induces also a concentration of normal stresses in their vicinity. The bottom plate behaves as a beam stiffened by the foam and supported by several almost rigid mastic ropes. The different displacements in the normal direction (x) between the two sides of the slit behind the upper corrugation induce necessarily a slight rotation downwards of the corrugation and of the inner wooden wedge.

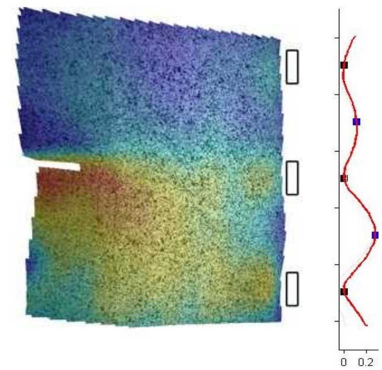

Figure 15 – Deformed foam with coloration according to normal strains (left). Deformed back plywood plate (red line on the right) - Instant t=-0.29 ms. Both obtained from post-processing of two high speed cameras inside the wall (optical system).

Comparison of the loads on the two blocks

The different local loading processes on the rigid block have been described in detail in the previous section. **Figure 13** summarizes all pressure signals recorded by the pressure sensors RP1 to RP8 on the same column of sensors of the rigid block (see **Figure 2** for the exact locations). The mirror column of pressure sensors on the Mark III block also had 8 sensors MP1 to MP8. Their locations are shown in **Figure 2** and **Figure 14**. Unfortunately four of them were out of order during test 140. Sensors MP1, MP4, MP5 and MP8 were working satisfactorily. Their time traces are shown in **Figure 16**.

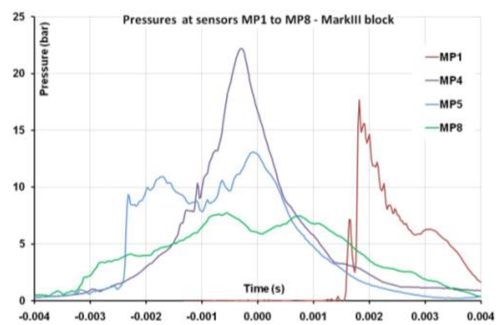

Figure 16 – Pressure signals at MP1, MP4, MP5, MP8 on the Mark III block.

The same main events happened in front of the Mark III block as in front of the Rigid block although a few millisecond earlier, as already mentioned. The reattachment of the flow to the wall, after separation from the middle corrugation, induced the entrapment of an air pocket in between the middle corrugation and the reattachment point. MP8 was inside the pocket or close to its boundary. Signals at MP8 and RP8 are therefore very similar. There was no working sensor available at the reattachment location (around MP7) and thus the much localized pressure pulse due to the impact was not captured. But from the impact point arose an upward vertical jet. The quick rise of the MP5 pressure signal at -2.5 ms is due to the root of the jet passing by the sensor. The same kind of traveling pulse at the root of a vertical jet was also seen on pressure sensors RP6, RP5 and RP4 of the rigid block.

The main difference between the two blocks is that the reattachment on Mark III side also entrapped a gas pocket below the upper corrugation. Both MP4 and MP5 were inside the gas pocket at the reattachment time, which explains that they recorded the same pressures until MP5 went out of the pocket around -2.5 ms. It can be checked on **Figure 13** that the sharp rise of pressure due to the traveling pulse on signals RP6, RP5 and RP4 started from a null pressure, which proves that the air around could escape quickly enough and thus that there was no gas pocket below the upper corrugation of the rigid block.

The presence of a gas pocket underneath the upper corrugation of the Mark III block also explains the significantly smoother pressure peak at MP4 compared to RP4 even though the maximum pressure obtained is not only due to the compression of air.

This local difference of the loading processes could be explained by 3D effects, as only a tiny difference on the incident flows would be needed to make it. In that case, the reduction of maximum pressure on Mark III block with regards to the rigid block would be pure chance. Nevertheless, one can also consider that the entrapment of the gas pocket underneath the upper corrugation has been favored by the receding of the primary foam and the rotation downwards of the corrugation. This could thus have been considered as a result of the fluid-structure interaction on the Mark III panel. The hydro-elasticity would not only be a simple mass/spring issue but could also cause the switch between different local loading processes.

Time traces of strains in the Mark III panel

There are five different parts in the Mark III structure that should be scrutinized separately: the plywood top plate, the foam (primary and secondary), the plywood back plate, the triplex sheet and the mastic ropes. Due to the concision requested for a conference paper, only the first three parts, considered as the weak structural points, are presented. For the triplex sheet, it is apparent that its influence is moderate as there is no discontinuity of the normal strains in the foam in its vicinity (see **Figure 15**). Only a selection of signals among many others is presented here in order to give a sense of what is considered to have really mattered during the impact.

- **Top plate**

Figure 17 presents the strain time traces as measured by the strain gauges underneath the plywood top plate (ST1 to ST8, see **Figure 14**). These are longitudinal strains, the direction of the gauges being vertical. Positive strains mean tension of the lower fibers.

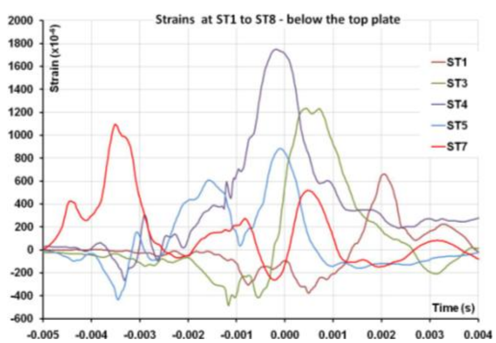

Figure 17 – Strain (microstrain) time traces measured by gauges ST1 to ST8 under the top plate of the Mark III block.

The signal ST2, ST6 and ST8 have been voluntarily excluded of **Figure 17** for the sake of readability and because they did not bring much insight. Reference is made to **Figure 16** for comparison with the pressure signals on sensors MP1, MP4, MP5 and MP8 on top of the plate. Colors are the same for signals from strain gauges and pressure sensors at the same height.

The strains in **Figure 17** are most of the time positive (tension of the fibers) because the main events (reattachment near MP7 and strong compression of the gas pocket under the corrugation) lead to a local bending of the top plate which has to be counterbalanced further by an opposite bending inducing a global dynamic behavior of the plate. This is particularly clear when looking at ST7 strain around -0.7 ms: while the load is increasing quickly just below the slit, the shape of the plate is forced to accommodate at ST7, far from the event.

The response at ST4 follows closely the load at MP4. This gauge gives the maximum strain which is still low ($1.8\ 10^{-3}$). It is reached only with a small delay (0.2 ms) after the maximum at MP4.

Due to the relaxation slit behind the corrugations, the top plate is split in independent parts vertically. Strains at ST1 to ST3 above the upper slit and at ST4 to ST8 below the upper slit should be largely decoupled as they are located on two separate parts of the plate. Actually, the drop of the strain on gauge ST3 while the pressure rises at MP4 (and thus the strain rises at ST4) indicates that the corrugation and its inner wooden wedge transmit a part of the load to the upper part of the plate which tends to bend its edge towards the interior of the panel.

These signals bring indirect information about loading processes that could not been recorded directly because of broken pressure sensors (MP2, MP3, MP6, MP7): (1) the reattachment after the flow separation from the middle corrugation that was captured on the rigid block by sensor RP7 (see **Figure 8**) occurred also on the Mark III panel. The first two peaks of ST7 are the response of this impact; (2) the reattachment after the flow separation from the upper corrugation that was captured by sensor RP3 (see **Figure 8**) occurred also on the Mark III panel around broken sensor MP3. The large peak around t=0.5 ms is the consequence of this impact. The peak of ST1 around t=2 ms is due to the passage of the root of the vertical jet (maximum just a little delayed compared to maximum of MP1) following the reattachment.

The accelerometers AT1 to AT8 located under the top plate show an intense dynamic activity from the impact due to the reattachment with a saturation of the sensors at around 400 g. Fast Fourier Transforms of both strains and accelerations do not show clear modes.

The maximum level of strain recorded in the whole top plate is 0.002 (0.2%).

- **Foam**

The post-processing of the images recorded at 15 kHz by the two high speed cameras inside the wall provides relevant information on the structural behavior of the Mark III panel like, for instance, the displacement, the strains in the main directions ε_{xx} (normal to the wall) and ε_{zz} (vertical), the shear strain ε_{xz} or ε_{zx}, and the acceleration at any point in the image. **Figure 18** shows the time traces of the normal strains at the six points through the thickness of the foam on the same horizontal line as sensor MP4 and on the same line as sensor MP5 (see **Figure 14** for the exact location of the points). Starting from the top of the top plate, the first point on a horizontal line is 30 mm away. The next points are located every 50 mm.

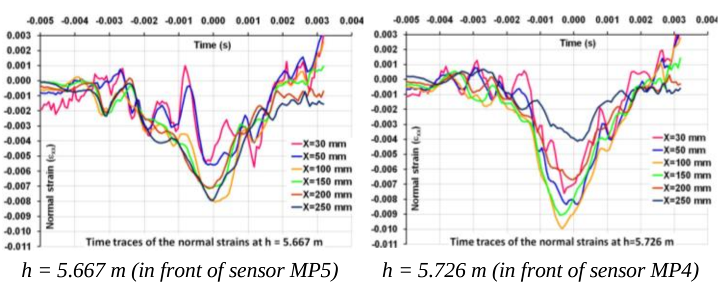

h = 5.667 m (in front of sensor MP5) *h = 5.726 m (in front of sensor MP4)*

Figure 18 – Time traces of the normal strains ε_{xx} as post-processed by the optical system at six points at the same height as MP5 (left), at six points at the same height as MP4 (right).

Negative values of the normal strain mean that the foam is in compression.

A simple verification of these values consists in comparing the mean value over a horizontal line (say, the line starting from MP4) at a time this value is at a maximum (mean(ε_{xx}) = -0.0074) with the difference of maximum displacements at the two ends of the line divided by the thickness of the panel ((0.5-2.5)/270=-0.0074).

The normal strain field at t=-0.29 ms, corresponding to the maximum pressure (recorded at MP4) and approximately to the maximal strain, is given in **Figure 15**. The coloration helps to understand the distribution of the strains in the foam and therefore the distribution along the two horizontal lines from MP5 and MP4. For instance, it can be noticed from **Figure 18** (left) that the maximum strains on the line starting from MP5 is reached after the maximum on the line at MP4, although the maximum load at MP5 is reached much before the maximum load at MP4. This is clearly due to a 2D behavior within the foam imposed mainly by the global dynamic behavior of the top plate leading to a spreading of the strain field from the load source. This influence of the top plate explains also a more dynamic behavior of the points in the vicinity of the top plate.

The maximum strain in the foam obtained from the optical system is around 1.5% just under the slit. We will come back on this point in the next section and compare it with the strength.

- **Back plate**

Figure 19 presents the strain time traces as measured by the strain gauges SB3 to SB7 alternatively on both sides of the plywood back plate in view of the optical system (see **Figure 3** and **Figure 14** for exact locations). These are longitudinal strains, the direction of the gauges being vertical. Positive strains mean tension of the fibers.

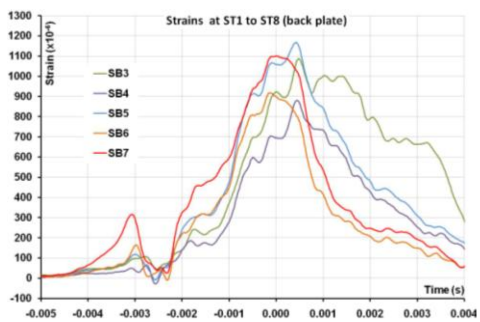

Figure 19 – Strain (microstrain) time traces measured by gauges SB3 to SB7, over and underneath the back plate of the Mark III block.

All strains are positive, which corresponds to the bending behavior of a beam stiffened by the foam supported by the rigid mastic ropes. Maximum strain in the whole back plate is around 0.002 (0.2%).

STRENGTH ANALYSIS

Before test 140, two tests had already induced large pressures though smaller than during test 140. A visual inspection had been conducted after these two tests and no deformation of the corrugations had been observed. Therefore, it is considered very unlikely that any deformation of the corrugations was present before test 140. After test 140 clear deformations of the small horizontal corrugations, but no deformations of the large vertical corrugations, were observed visually. A thorough inspection of the corrugations was carried out with precise measurements of the indentations. During this inspection no visible permanent depression of the membrane in front of the Mark III block was noticed. It was then decided to reproduce twice a moderate wave impact that had already been tested in order to compare the new strain measurements with the previous ones and detect a potential damage of the panel. As no clear modification was observed in the response of the containment system, it was decided to stop the test campaign and check carefully the foam and the plywood plates of the Mark III test panel.

This section describes the state of the Mark III test panel after test 140 through the results of the different investigations. Strength curves from static tests at ambient are provided for the different components of Mark III and a short analysis is done for a comparison between the Sloshel measurements and what would have been expected from these curves.

Small reinforced Corrugations

As already mentioned, the reinforced version of the membrane was used during the Sloshel Mark III test campaign. **Figure 20** (left) shows the distribution of the wooden wedges inside the small (horizontal) and large (vertical) corrugations. It can be seen that there is a gap of 80 mm in the central part of the small corrugations in between the two long wooden wedges.

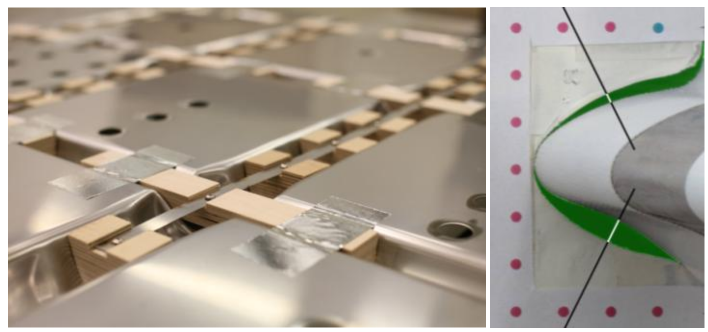

Figure 20 – Reinforcement of the primary membrane by wooden wedges (left) – Most deformed corrugation during test 140: comparison with a template (right).

Only three rows of horizontal corrugations, around the top part of the test blocks, presented visible deformations. All the deformations were in the form of dents on both sides of the corrugations but more pronounced on the lower side. The dents were visible only in the central part of the corrugation, where there was no support of the wooden wedges. No upward or downward global bending was noticed.

The measurements of the indentations for each corrugation of the three rows were performed with the help of a template made directly with a spare part of the primary membrane (overlap membrane part). The template was put over the deformed corrugations as shown in **Figure 21** (left).

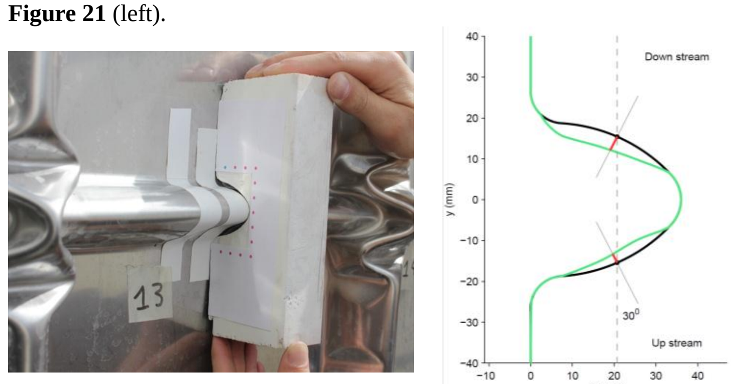

Small corrugation template *Definition of the indentations*

Figure 21 – Measurement of the indentation of horizontal corrugations.

Photos of the gap between the template and the deformed corrugation were made and post-processed in order to derive two values of deflections according to GTT's recommendations as shown in **Figure 21** (right). The uncertainty on the final result was estimated to be plus or minus 0.5 mm.

The maximum indentation measured was 5 mm on the lower side of an upper corrugation of the rigid block, just above pressure sensor RP48. This sensor recorded a maximum pressure of 51.7 bar. The upper side of the corrugation was also the most deformed with an indentation of 2 mm. The picture obtained during the inspection for this corrugation is presented in **Figure 20** (right) after geometrical correction by reference to the locations of the pink dots.

The permanent deformations on both sides of all the horizontal corrugations together with the maximum pressure measured by the sensors are presented in **Figure 22**.

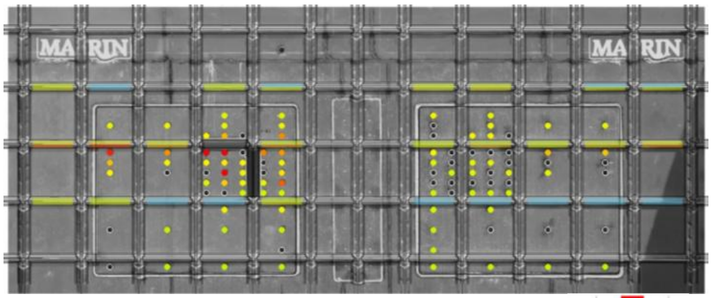

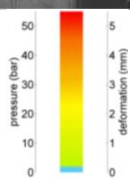

Figure 22 – Indentations on both sides of the horizontal corrugations and maximum pressure recorded by the sensors. Colour scales are given on the right.

When the corrugation is coloured in blue, it means that no visible deformation was observed. A quick look at **Figure 22** allows one to notice that both the pressures and the permanent deflections on the corrugations are lower on the Mark III block than on the rigid. It is difficult to determine conclusively whether this is due to a fluid-structure interaction influence or simply to 3D effects. Nevertheless, it is interesting to notice that the maximum deflections on the lower side of the upper corrugations of the Mark III block range from 1.5 to 2.8 mm whereas the corresponding deflection is 3.8 mm on the next corrugation on the right of the wall lying directly on the concrete. One could argue that it is due to boundary effects along the wall but this increase of deflection does not exist on the other side of the wall.

Bogaert et al. (2010), describing a similar Sloshel test campaign but at a scale of 1:6, mentioned that there is a correlation between the upstream pressure close to a horizontal corrugation and the vertical force measured on this corrugation even though the distance to the corrugation has obviously a large influence on the pressure result. It is therefore interesting to compare the permanent deformation measured on the down side of a horizontal corrugation to the maximum upstream pressure measured by the closest sensor when available. **Figure 23** shows the results for the seven deformed corrugations having an upstream pressure sensor in their vicinity (distance of 50 mm between the sensor and the centre of the corrugation).

All the deformations and corresponding pressures on the Mark III panel are lower than those on the rigid block for the upper line of corrugations (RP09 is located below the middle corrugation).

The curve in red on **Figure 23** is a strength curve of the small reinforced corrugation obtained from static tests at ambient temperature. The pressure was uniform around the corrugation during the tests and the deformations were symmetrical.

There is a good linear correlation between the deflection and the maximum upstream pressure. Although the minimum visible permanent deformation (around 2 mm) was obtained for an upstream pressure very close to the static pressure for the same deflection, the trends given by the two curves diverge progressively when the pressure increases: to obtain a given deformation, a much lower static pressure is needed than the maximum dynamic pressure measured upstream of the corrugation during test 140.

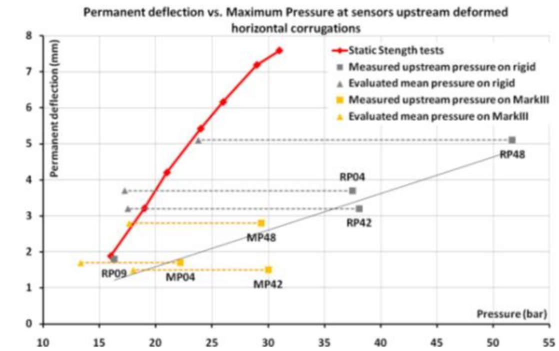

Figure 23 – Permanent deflection of horizontal corrugation vs. Maximum measured upstream pressure (square dots) and maximum evaluated mean pressure (triangles). Labels of the pressure sensors are given. Yellow dots for Mark III, grey dots for Rigid. Static strength curve in red.

Two different reasons could be proposed: (1) the spatial distribution of the load on the corrugation; (2) an increase of the strength due to the load rate.

For the first reason, one has indeed to consider that the pressure measured at the root of the corrugation is very high but in a strong region of the corrugation. The local pressure could be much lower in the central part of the lower corrugation side, which is structurally more sensitive. The corrugation sensor just above sensor RP27 can give some insight about this point. The maximum pressure at RP27 is 55.5 bar. The maximum vertical upward force measured by the corrugation sensor is 25.6 kN (see **Figure 12**). As the length of the corrugation is about 270 mm and its height is 37.2 mm, the surface on which the mean pressure is to be calculated is 0.01 m^2. It means that the value of the force in kN is precisely the value of the mean pressure in bar. Therefore, the maximum mean pressure on the corrugation sensor is 46% of the maximum upstream pressure. This ratio should be relevant for all upper corrugations on the rigid block as they withstood the same kind of loading process. Assuming this ratio for defining a relevant pressure associated to the permanent deformations of the upper corrugations of the rigid blocks leads to a move of the grey square-shaped dots of **Figure 23** until the grey triangles. These new locations match reasonably well with the static strength curve at ambient. For such a comparable match for the corrugations on Mark III a ratio around 60% is to be assumed. The orange square dots are thus replaced by the orange triangles.

Such ratios fit rather well with the local loading processes proposed for the two blocks. Indeed the compression of an entrapped gas pocket underneath the corrugation (Mark III block) would lead to an almost uniform pressure underneath the corrugation on a large part of it. Having a smaller ratio for the compression of an escaping air jet is expected as the pressure at the free end of the jet is the atmospheric pressure.

Therefore the distribution of the loads below the upper corrugations is enough to explain the difference between the static strength curve and the strength curve from test 140 built simply from the maximum upstream pressure. No special increase of strength due to a load rate influence is required. The static strength curve of the reinforced horizontal corrugations at ambient temperature is therefore relevant for highly dynamic impacts: for a given deflection during an impact, the related pressure from the curve gives a valuable estimation of the maximum average pressure really withstood by the corrugation.

Mark III panel (foam + plywood plates)

The Mark III block used for the Sloshel campaign was a reinforced version: the spaces between adjacent mastic ropes was 100 mm instead of 140 mm for the standard version.

- **State of the Containment system (plywood and foam)**

After the test campaign, the Mark III panel was dismounted and sawn into 16 blocks, through the slits of the primary foam behind the corrugations. Every side of the blocks was carefully inspected visually, by several Sloshel partners, especially in the vicinity of the slit where plastic deformation were expected. No crack or residual deformation was detected either in the plywood plates or in the foam.

Some small samples of foam were cut in the areas where plastic deformation had been expected and static compression tests were performed for comparison with static tests carried out before the campaign. The results in term of Young modulus and offset yield stress (0.2%) were not significantly changed and all in the usual range of characteristics. The conclusion was that the Mark III panel was essentially intact after all Sloshel tests and therefore after test 140.

- **Comparison of measured Strains and Strength from static tests at ambient temperature: Strain rate influence**

Table 1 summarizes the maximum absolute transient values for the relevant strains as measured (1) below the top plate, (2) on the section of the foam in view of the optical system and (3) on both sides of the back plate, together with the different material characteristics (offset (0.2%) yield strain (ε_0) and Young modulus (E)) obtained from static tests at ambient. For the plates, the strains are the longitudinal ε_{zz} strains measured by all gauges available (see **Figure 3**). For the foam, the strains are the normal ε_{xx} strains as deduced from the optical system on all points in view of the cameras.

Table 1 - Maximum strains in the Mark III panel and characteristics of materials from static tests at ambient

	Max(ε_{zz})	Max(ε_{xx})	ε_0	%ε_0	σ_0 (Bar)	E (Bar)
Top plate	0.002	-	0.007	29%	700	100000
Foam	-	0.015	0.02	75%	14	780
Back plate	0.002	-	0.007	29%	700	100000

ε_0, σ_0: offset yield strain and stress (0.2%)

The utilization factor of the static strength at ambient, defined as the ratio of the maximum strain to the maximum corresponding offset yield strain, is around 30% for both plywood plates and 75% for the foam. It must be kept in mind that for the foam we have only information on a boundary section where the maximum load recorded was only 2/3 of the maximum recorded on the Mark III panel. If we considered the most highly loaded section and applied a magnification factor of 3/2 on the corresponding strains, the utilization factor would be 113%. Therefore, in the vertical boundary section observed by the two high speed cameras of the optical system, the static strength was sufficient to withstand the load without any plastic deformation. But in more inner sections, small areas in the foam below the upper slit should have experienced plastic deformations if only the static strength was available. This means that the strength was higher than the static strength at least in the most loaded areas.

Now, the maximum strain rate in the foam derived from the optical system data was around 10 /s. The highest values were obtained just under the upper slit. At the level of pressure sensor MP4, namely 50 mm underneath the slit, the strains shown in **Figure 18** (right) have a highest rate of 7 /s. For a strain rate around 10/s, the Young modulus is quite similar (slightly increased) compared to quasi-static conditions, whereas the offset yield stress is highly increased. Therefore, in the local areas concerned by such a strain rate (just behind the top plate), the higher strength of the foam due to the strain rate influence prevented any plastic deformation into the foam.

However this strain rate influence does not explain the low level of strains measured.

- **Influence of the dynamic behavior of the top plate on the load distribution**

Figure 24 shows the normal stresses σ_{xx} into the foam at six points on a horizontal line starting from pressure sensor MP4, five centimeters below the slit behind the upper corrugation. The reference points are shown on **Figure 14**. The strains have been presented at the same points on **Figure 18**. The stresses have been deduced from the strains using the Young modulus in **Table 1**, obtained from static tests at ambient. This is relevant because the Young modulus does not change much for strain rates lower than 10 /s. The pressure at MP4 has been added on **Figure 24** as it is also the normal stress on the skin of the top plate at MP4.

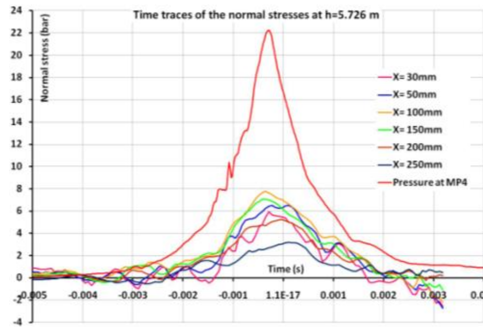

Figure 24 - Time traces of the pressure at MP4 and of the normal stresses σ_{xx} at six points at the same height as MP4.

There is a strong attenuation of the normal stress from the skin of the top plate (x = 0) to the first point in the foam in view of the optical system (x = 30 mm). The reduction factor is 3.6 when the pressure is at its maximum at MP4. It can also be noticed that the oscillations of the strains are stronger close to the plate than further into the foam but these oscillations are not clearly correlated with those at the strain gauge ST4 under the top plate on the same horizontal line.

What would have been expected from a more traditional analysis with only the records from the pressure sensors? A first well known reason for a reduction of stress into the foam is the distribution of the load by the cover plate. A current approach (see LR Sloshing Assessment Guidelines, 2009 or Gervaise, 2009) proposes to compare the mean maximum pressure calculated on different loaded areas (loading curve) to a static strength curve evaluated by static tests with patch loads. The pressure may be corrected by a Dynamic Amplification Factor evaluated by Finite Element dynamic analysis for different rise times of the load. Such a static strength curve takes benefit of the load distribution by the cover plate.

Let us first construct a loading curve: the minimum loaded area considered is 0.06 m x 0.06 m=0.0036 m^2, which corresponds to the area of influence of a single pressure sensor (60 mm between sensors). The maximum pressure to be considered for this smallest area is 30 bar obtained on sensor MP42. In contrast, when considering the entirety of the Mark III panel, an associated peak pressure may be calculated as peak transient force, namely 726 kN as measured by the load cells behind the panel, divided by associated area, namely 1.2 m^2, which gives 6 bar. The intermediate areas have been chosen considering a row of sensors (area: 0.08 m x 1.2 m=0.096 m^2; mean pressure from MP4, MP42 and MP48=20 bar) and a more complete collection of sensors (0.33 m^2, 11 bar).

For choosing a strength curve a special attention must be paid to the criterion. Criteria adopted on board ships can be related to two limit states: (1) failure of the back plywood in between two mastic ropes by shear or bending fracture. The criterion for the strength is a maximum residual deflection of 0.5 mm of the back plywood; (2) fatigue of a membrane knot by rotation when not well supported due to foam crushing – the criterion for which is 10 mm crushing. GTT has built several experimental strength curves by static tests of the standard and reinforced version of Mark III with patch loads at ambient or in service conditions. At ambient and for a standard version of Mark III, the criterion on the back plywood is more severe and thus the tests are conducted with several displacement sensors located behind the back plywood. The foam is checked at the end of the tests. Such a strength curve would provide significantly higher values than the loading curve for test 140 but would not help understanding. For the reinforced version the foam crushes before the failure of the back plywood occurs but there is no experimental strength curve available at ambient temperature. Therefore, for the purposes of this paper we propose a strength curve based on numerical simulations for the reinforced version at ambient temperature. The criterion chosen is the occurrence of a first plastic deformation into the foam.

The loading curve for test 140 and numerical strength curve at ambient temperature are presented on **Figure 25**. A numerical strength curve based on the same criterion of no plastic deformation into the foam but with a thermal gradient from -162°C on the membrane to 20°C at the mastic ropes level has also been added.

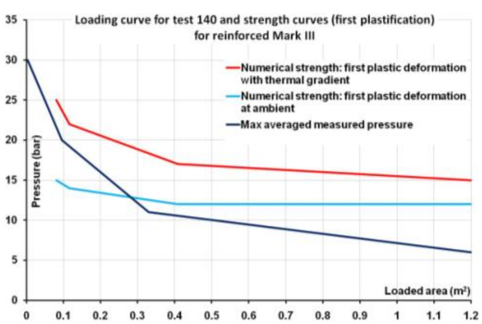

Figure 25 – Loading curve from test 140 (dark blue) - Numerical static strength (first plastic deformation) for reinforced Mark III panel at ambient (light blue) and with a thermal gradient in the Mark III panel (red).

This approach appears to be conservative as for the small loaded areas large zones of plastic deformation into the foam would have been expected from the strength curve at ambient temperature, which was not the case in reality. With an in-service thermal gradient of temperature through the thickness of the foam, the strength would increase significantly when considering smaller and smaller patch loads - this is not the case at ambient temperature. It suggests that the distribution of the load for small patches is efficient at cold temperature but not at ambient, due to a stiffening of the foam at low temperature which limits the local bending of the top plate. Therefore, the distribution of the load by the top plate seems not to be the right explanation for the low level of strains during test 140, at least when the spatial distribution of the loads is made by averaged patch loads.

A 2D Finite Element (FE) model of a vertical section of the Mark III panel was built in order to perform static and dynamic calculations and compare both behaviors. The linear material properties of the plywood and the foam described in **Table 1** were adopted. The plywood plates and the foam were discretized with 10x10 mm^2 elements. Static and dynamic calculations were performed with a load uniformly distributed on a patch area of 80 mm just under the upper slit. For the dynamic calculation, the load was given directly by the pressure recorded at sensor MP4. For the static calculation, a load of 22 bar, corresponding to the maximum pressure at sensor MP4, was applied.

Figure 25 shows the results in terms of normal stresses for both calculations. The black area corresponds to higher stresses than the offset yield stress for static tests at ambient (14 bar).

For both calculations, there is a large area under the slit for which the offset yield stress is exceeded. No reduction of stress behind the top plate is noticed. Moreover, there is a significant amplification of the strains into the foam when considering the dynamic load and therefore the *black area* is even larger. The maximum displacements under the slit are respectively 5 mm for the static calculation and 5.9 mm for the dynamic calculation, to be compared to the 2.6 mm obtained in reality. Whatever the size of the loaded area, the patch load approach would always lead to a dynamic amplification (even small) of the strains. Only for very small rise times (lower than 0.2 ms) a dynamic attenuation might occur. This is not the case here as the rise time of pressure sensor MP4 is larger than 1 ms. Therefore, the dynamic behavior of the plywood plates and the foam does not seem to be the right explanation for the attenuation of the strains behind the top plate, at least when the spatial distribution of the loads is made by averaged patch loads.

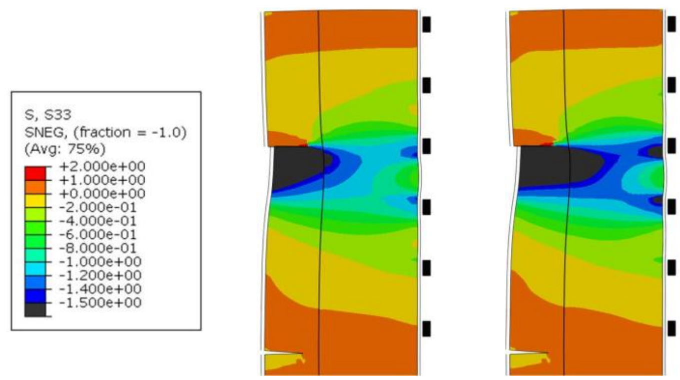

Scale for stresses (Mpa) *Static* *Dynamic*

Figure 25 – normal stresses in the foam calculated by static and dynamic FEA on a 2D model of Mark III reinforced panel with a patch load on an area of 80 mm under the upper slit. Dynamic load = pressure recorded at MP4. Static load= 22 bar = max at MP4.

Whichever the way a static load would be interpolated from the sensor signals MP4, MP5 and MP8 when pressure at MP4 is at maximum, the resultant strains would be significantly higher, but for a larger loaded area, thus for a smaller strength, as it has been verified with several calculations. So, a better spatial distribution of the loads does not appear to explain the attenuation of the strains into the foam at least for static loads.

All the above results combine two main parameters: (1) the spatial distribution of the loads (patch load/real distribution); (2) the dynamic behavior (static/dynamic). The results of test 140 indicate that there is an attenuation of the strains into the foam when the load is correctly distributed in space and time. Other results obtained by calculations for simplified spatial or time distributions are summarized in **Table 2** by an amplification factor of the maximum deflection *with regards to the measured one*. These factors are given here just as an indication of a general trend related to possible simplifications of load modeling.

Table 2 – amplification factors on the maximum displacement from FE calculations for different simplifications of the load modeling for test 140.

	Static load	**Real time distribution**
Patch load	1.8	2.1
Real space distribution	3.0	1

The simplifications of the spatial and time distributions of the loads that are commonly used lead to an overestimation of the strains into the foam and of the maximum displacement for the conditions of test 140. Therefore only a realistic dynamic loading with explicit FE calculations on the whole loaded area should be able to explain the real results.

This is not as simple as it could be first thought because the knowledge on the load through the pressure sensors is incomplete. For instance, among the eight sensors (MP1 to MP8) on the same column, that are of interest for the behavior of the foam in view of the optical system, only 4 sensors were working correctly and a major event such as the reattachment of the flow on the wall after its separation from the middle corrugation was not captured. Even with a complete column of close working sensors, as shown in Figure 6 for the rigid block, the continuity between the signals is not obvious and a relevant interpolation is not straightforward. Nevertheless work is in progress on this matter.

It is believed that when considering a realistic time-space distribution for such globally upwards traveling loads obtained with breaking waves, the dynamic bending behavior of the top plate stiffened by the foam is different than with patch loads and leads to a much better distribution of the loads into the foam. It appears as though the high frequency content of the pressure peaks were filtered by the global dynamic behavior of the top plate.

CONCLUSIONS

During a Sloshel wave impact campaign in a flume involving a fully instrumented reinforced Mark III panel, a Flip-Through impact inducing high pressures was generated (referred to as test 140). Such a Flip-Through impact is considered to be very unlikely on board a LNG carrier but the highly dynamic loading conditions it generates bring insight about fluid-structure interaction in extreme conditions.

During a Flip-Through, the moving forward of the wave front and the run-up of the wave trough progress simultaneously until the front and the trough meet in a very restricted area (*restricted trough* conditions).

The combined analysis of the pressure signals and the videos from high speed cameras watching closely the impact through an observation window enabled the decomposition of the loading mechanisms.

The elementary loading processes (ELP) appear to be very general as far as wave impacts on a structure are concerned. They are: (1) the actual impact (discontinuity of velocity), very localized and inducing acoustic pressure with the local velocity of sound of the aerated water; (2) the building of a jet along the wall from the impact area. The sharp turn of the velocities induces a traveling pressure pulse at the root of the jet; (3) the compression of entrapped gas pockets or escaping gas jets.

All these processes generate loads directly in their vicinity. They have also a more remote influence transmitted by pressure waves through the fluids.

In the particular case of test 140, the situations in which the ELPs developed are related to the nature of the impact (Flip-Through) and to the interactions with the corrugated membrane are: (a) violent reattachment of the flow after separation from a corrugation during the trough run-up (ELP1); (b) building jet from the reattachment point (ELP2); (c) compression of the gas pockets entrapped above the corrugation during the reattachment or entrapped in between the reattachment point, the wave front and the upper corrugation (ELP3); (d) impact of the jet on the root of the upper corrugation (ELP1); (e) compression of a jet of escaping gas below a corrugation (ELP3).

The development of different kinds of free surface instabilities appears to be also a general process associated to wave impacts - these are: (1) Kelvin-Helmotz (KH) instabilities due to the tangential jet of escaping gas; (2) Rayleigh-Taylor (RT) instabilities when entrapped gas tends to penetrate the free surface.

During test 140, KH developed during the forward move of the wave front and also below the corrugations. It is believed the KH instability is the main cause of the non repeatability of wave impact pressure measurements even on a flat wall. RT developed underneath the upper corrugation during the final compression of the escaping air jet or the entrapped air pocket. RT might be a mitigating process preventing higher compression. RT creates locally clouds of fine bubbles which eventually increase the aeration of the water. Both phenomena should be studied further in the context of sloshing as they seem to have a large influence on the impact pressures.

The maximum pressure recorded on the rigid block was 56 bar whereas it was 30 bar on the Mark III panel. In both cases the maximum pressure occurred under the upper corrugation. Although the flow was predominantly 2D, the loading processes involved were different on the rigid block and the Mark III panel. On the rigid block, the gas was escaping until the last moment whereas it was entrapped much earlier on the Mark III panel. This difference was considered to be the main reason for the discrepancy on the maximum pressures. It could be simply attributed to small 3D variations of the flow. Nevertheless, the entrapment of gas was favored by the receding of the foam just below the upper corrugation and the related rotation of the corrugation. Therefore, the gap between the maximum pressures could also be attributed to fluid-structure interactions. In such a case, hydro-elasticity appears as more complex than a mass/spring system interacting with a given wave loading process, and could be the cause of a switch from one loading process to another.

Three rows of horizontal reinforced corrugations were deformed during test 140. The vertical corrugations were not deformed. Indentations on both sides of the horizontal corrugations occurred in their central part where there was no support from the wooden wedges. The deflections were significantly more pronounced on the lower side. No global bending of the corrugations was observed. Maximum measured deflection was 5 mm.

This type and level of permanent deflection of the membrane corrugations is not considered as damage since fatigue tests conducted by GTT have shown that deformed corrugations still behave in the same way as non deformed corrugations and their lifetime is not shortened.

The level of deflection is clearly correlated to the maximum upstream pressure (50 mm below the center of the corrugation, thus very close to the foot of the corrugation). Consequently, the deflections are lower on the Mark III panel than on the rigid block. As on both sides of the Mark III panel the deflections on the rigidly supported corrugations are larger than on the Mark III supported corrugations, hydro-structure interaction appears to be a better explanation than random 3D effects.

The maximum mean pressure on the lower side of a corrugation is lower than the corresponding maximum upstream pressure. The ratio deduced from comparison between the force measurement by the horizontal corrugation sensor and the upstream pressure measurement (sensor RP27) is 46%. This ratio should be relevant for all upper corrugations of the rigid block as the loading process remains the same. When applying this ratio to the measured upstream pressures for defining a relevant pressure corresponding to a deflection of any horizontal upper corrugations of the rigid block and to be compared with the strength curve obtained by GTT with static tests at ambient, the points match rather well with the curve. For a comparable match with the corrugations on Mark III a ratio of 60% is suggested. These ratios fit quite well with the two loading processes proposed for the rigid block and Mark III panel, namely the compression of respectively a jet of escaping air or an entrapped gas pocket. Therefore, considering a static strength curve for the corrugations appears to be relevant: no special reinforcement due to a load rate influence appears to be needed to be taken into account.

Although having experienced local pressures of up to 30 bar, exceeding by far the offset yield stress in quasi-static conditions at ambient temperature, the foam of the Mark III panel did not exhibit any discernible cracking or discernible plastic deformation area after the test, according to visual inspection after cutting the panel in 12 blocks and according to material tests on small samples.

From the post-processing of the optical system measurement, the strains exceeded the quasi-static offset yield strain inside the foam, at least locally under the relaxation slit behind the upper corrugation. As the strain rate in this area was around 10 /s and as the strength (offset yield strain) of the foam is much larger for this range of strain rate, the dynamics of the material played a clear positive role to prevent any plastic deformation.

Moreover, the maximum transient displacement deduced from the optical system measurements was only 2.6 mm. A significant attenuation of the stress level just behind the top plate was observed which could not simply be explained by just the dynamics of the material, as the Young modulus was only moderately increased for the considered range of strain rates. It appears that the pressure signal was filtered by the top plate stiffened by the foam.

According to the current approach, consisting of comparing maximum averaged pressures on different loaded areas (loading curve) to strengths obtained under corresponding quasi-static patch loads (strength curve), the most relevant loading areas for test 140 are the small areas for which the load exceeds the strength. For such areas chosen just under the upper slit, the distribution of the load by the cover plate turns out not to be efficient at ambient temperature. Finite element calculations with the maximum averaged pressure on this area would lead to a large overestimation of the maximum displacement. Introducing the dynamics of the load would amplify the maximum displacement. Introducing the spatial distribution of the loads for quasi-static conditions would lead to an even worse theoretical result.

It seems that only a realistic distribution of the load in space and in time can lead to the actual structural response. This can unfortunately not be easily tested by FE calculations because the density of working pressure sensors is too scarce for a relevant interpolation of the load in space and time domains. Fully coupled fluid-structure interaction analysis (FSI) is seen as a way forward. Nevertheless some efforts are being made to reconstruct the actual interpolated load by an iterative process taking benefit of the knowledge gained from the loading process analysis.

Finally it is interesting to note that the Mark III structural behavior seems to adjust favorably to the worse in service conditions, by:

- large increase of the elastic domain for strain rates around 10 /s;
- strain attenuation for a realistic space and time distribution of the load, at least in case of highly dynamic loading conditions;
- better load distribution by the top plate under cryogenic temperatures;
- large increase of the Young modulus and of the offset yield stress of the foam under cryogenic temperatures.

ACKNOWLEDGEMENTS

The views expressed in the paper are those of the authors and do not necessarily represent the unanimous views of all the Sloshel consortium members.

The authors would like to acknowledge the support provided by the Sloshel consortium members that have made the Sloshel project possible: American Bureau of Shipping, Bureau Veritas, Ecole Centrale Marseille, Chevron, ClassNK, Det Norske Veritas, GDF SUEZ, GTT, Lloyd's Register EMEA, MARIN, Total and Shell.

REFERENCES

Bogaert, H., Brosset, L., Kaminski, M.L., (2010) "*Interactions between wave impacts and corrugations of Mark III Containment System for LNG carriers: findings from the Sloshel project*", 20th (2010) Int. Offshore and Polar Eng. Conf., Beijing, China, ISOPE.

Brosset, L., Mravak, Z., Kaminski, M., Collins, S., Finnigan, T., (2009) *"Overview of Sloshel project"*, 19th (2009) Int. Offshore and Polar Eng. Conf., Osaka, Japan, ISOPE.

Carden, E.R., Maguire, J.R., Durley-Boot, N.J., (2011) "*Modal testing and model reconciliation of the Sloshel Mk III test panel*", 21st (2011) Int. Offshore and Polar Eng. Conf., Maui, (HI), USA, ISOPE.

Drazin, P.G., Reid, W.H., "*Hydrodynamic Stability*", Cambridge University Press, 2004

Gervaise, E., de Sèze, P.E., Maillard, S., (2009) *"Reliability-based methodology for sloshing assessment of membrane LNG vessels"*, 19th (2009) Int. Offshore and Polar Eng. Conf., Osaka, Japan, ISOPE.

Hofland, B., Kaminski, M.L., Wolters, G., (2010) "*Large Scale Wave Impacts on a Vertical Wall*", 32nd Int. Conf. on Coastal Engineering, ICCE 2010, Shanghaï, China, June 30 – July 5, 2010.

Kaminski, M.L., Bogaert, H., (2010). "*Full-Scale Sloshing Impact Tests Part II*", 20th (2010) Int. Offshore and Polar Eng. Conf., Beijing, China, ISOPE.

Kaminski, M.L., Bogaert, H., Brosset, L., (2011). "*Full and large scale wave impact tests for a better understanding of sloshing – Results of the Sloshel project*", 30th (2011) Int. Conf. on Ocean, Offshore and Arctic Eng. OMAE 2011-49992, Rotterdam, the Netherlands

Kimmoun, O., Ratouis, A., Brosset, L., (2010) *"Sloshing and scaling: experimental study in a wave canal at two different scales"*, 20th (2010) Int. Offshore and Polar Eng. Conf., Beijing, China, ISOPE.

Lafeber, W., Brosset, L., Bogaert, H., (2011) "*Loads on Mark III corrugated primary membrane: findings from the Sloshel project*", 21st (2011) Int. Offshore and Polar Eng. Conf., Maui, (HI), USA, ISOPE.

Lloyds Register, (2009) "*Sloshing Assessment Guidelines (SAG), Version 2*", May 2009

Wagner, H., (1932) "*Uber Stoss- und Gleitvorgänge an der Oberfläche von Flüssigkeiten*", Z. Angew. Math. Mech. 12, pp 193-215 (English transl: "*Phenomena associated with impacts and sliding on liquid surfaces*", NACA Translation 1366.)